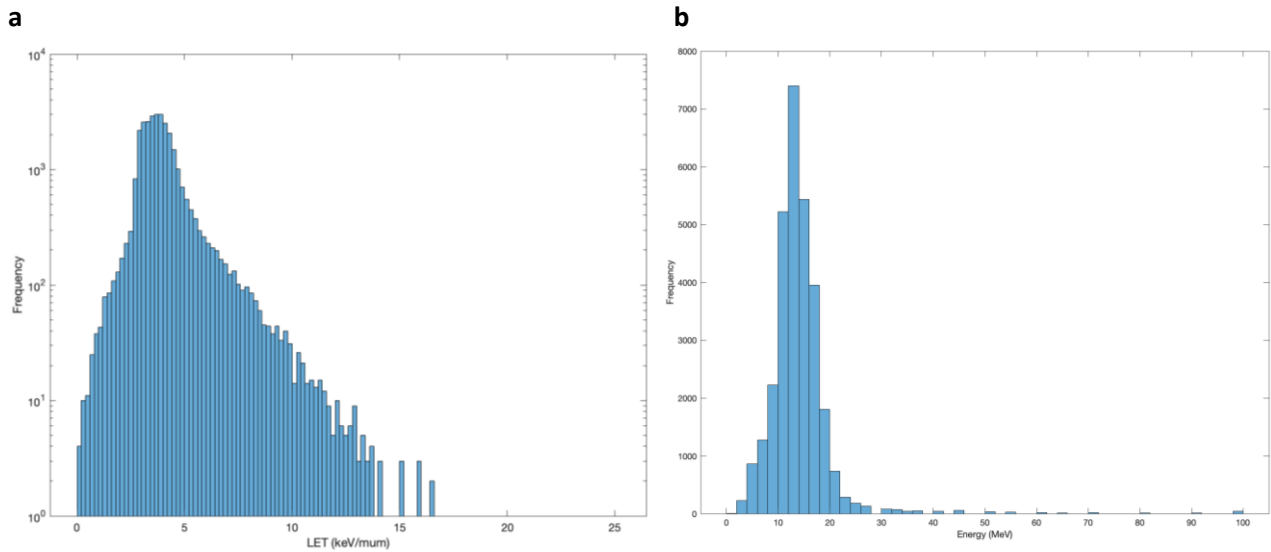


Supplementary Information of:

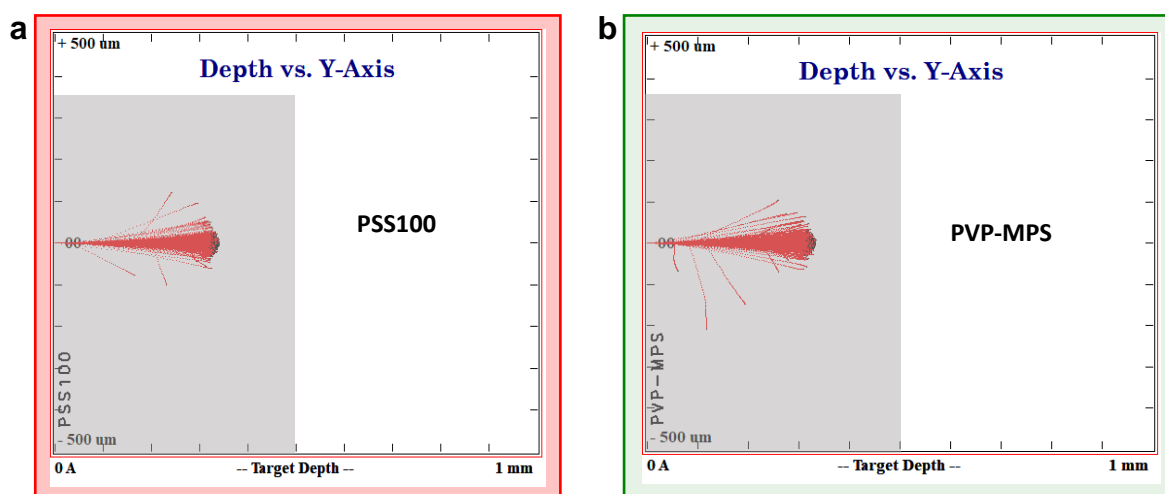
Flexible fully organic indirect detector for megaelectronvolts proton beams

Supplementary Note 1. Monte Carlo simulation for proton irradiation of prostate tumor



Supplementary Figure 1. Data distribution from MC simulations of a representative treatment plan for prostate tumor. The histograms report the dose-average LET distribution (**a**) and energy range (**b**) from the simulation shown in Fig. 1c-d of main text. According to current clinical practice, the energy range of incoming protons was considered 162-197 MeV from two opposing fields, the schedule plan of $2 \text{ Gy} \times 39$ fractions, the RBE for protons constant at 1.1.

Supplementary Note 2. Siloxane-based scintillators

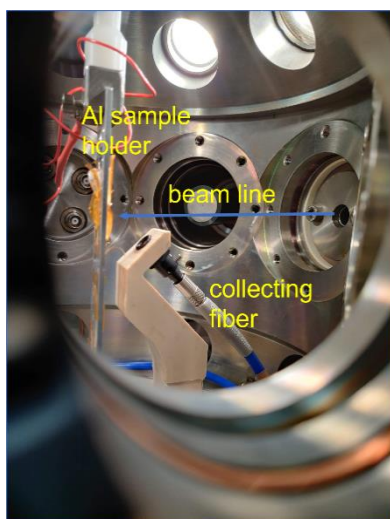


Supplementary Figure 2. SRIM simulation plot. Range of the 5 MeV proton beam inside the 0.5 mm thick PSS100 (a) and PVP-MPS (b) scintillating films.

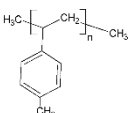
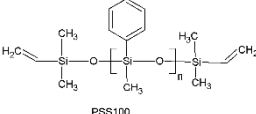
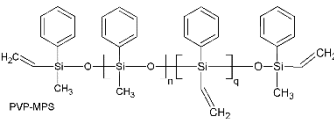
Plastic scintillator Primary and secondary dyes	Emission wavelength λ_{em} (nm)		reference
Primary dye - aromatic compounds	300 - 380		1
Wavelength shifters for blue-shift	430-450		1
Green-emitting wavelength shifter	540		1
Wavelength shifters for red-shift	600		1
Phototransistor Organic semiconductor			
	Optical absorption $\lambda_{abs,OSC}$ (nm)	Field-effect mobility μ_{FE} ($cm^2 V^{-1} s^{-1}$)	
pentacene	590 and 670	> 1	2,3
poly(3-hexylthiophene-2,5-diyl) (P3HT)	520	0.0001-0.1	4,5
dinaphtho[2,3-b:2',3'-f]thieno[3,2- b]thiophene (DNNT)	450	> 1	3,6,7
[6,6]-phenyl C ₇₁ butyric acid methyl ester (PC71BM)	375 and 480	0.1	4,5,8

Supplementary Table 1. State-of-the-art for plastic scintillators and organic semiconductors.

In the table are reported for comparison the main figures of merit to be considered for a proper matching of the scintillator and the OSC: the scintillator emission wavelength with the optical absorption wavelength of the OSC, the field-effect mobility of the semiconductor.



Supplementary Figure 3. INFN-LNL setup for IBIL spectra measurement.

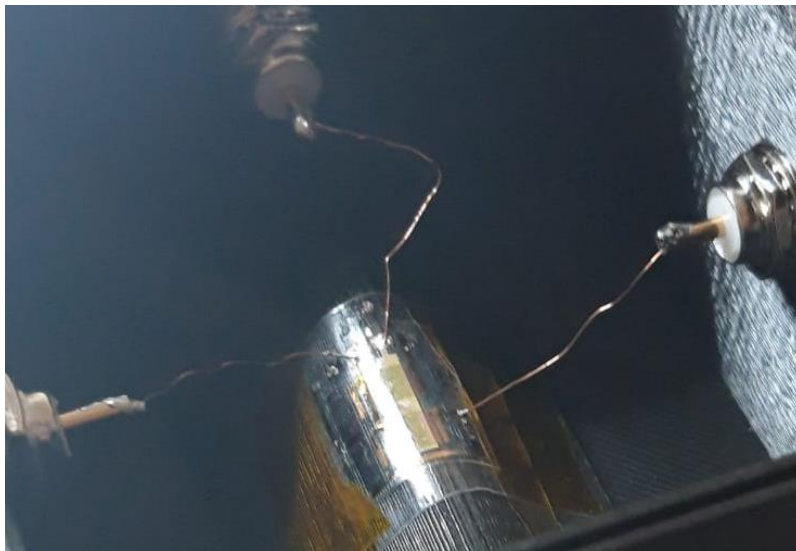
Label	Base resin structure	Phenyl groups (mol l ⁻¹)	Vinyl groups (mol l ⁻¹)	Dyes	Refractive index
EJ-212		8.5 ¹		Proprietary Eljen Technology	1.58
PSS100 polymethyl phenylsiloxane		7.6	0.89	PPO 2%, LV 0.02%	1.537
PVP-MPS polyvinylphenyl methylphenylsiloxane (n 30-40 %)		7.7	3.9	PPO 2% LV 0.02%	1.53

¹ Using MW 4×10^5 according to the literature ⁹.

Supplementary Table 2. Structures, labels and properties of the used resins and the commercial plastic EJ-212. The structures and main relevant features of the base resins used to produce organic scintillators are reported.

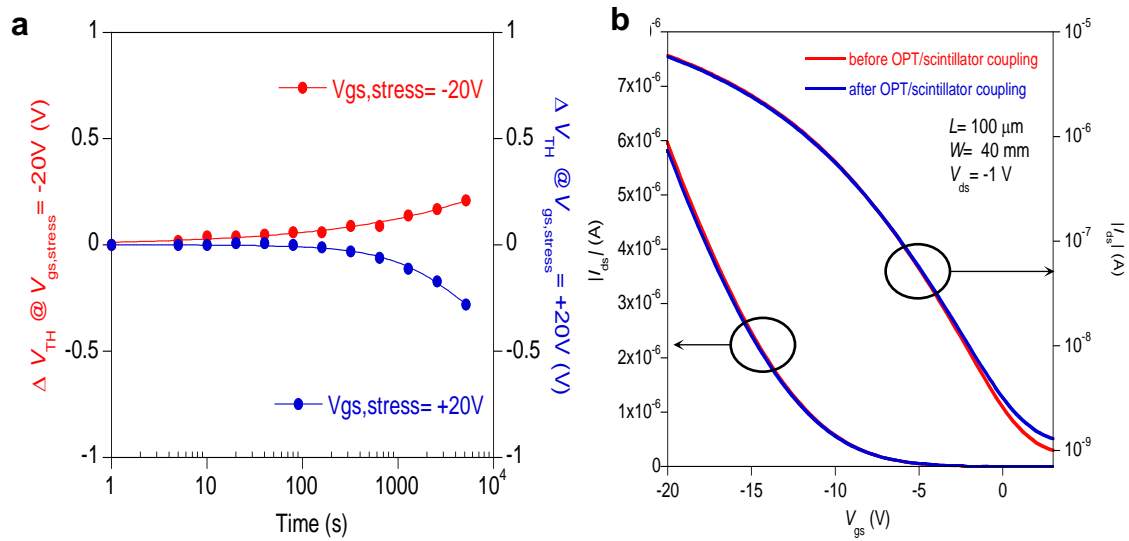


Supplementary Figure 4. Manufacturing process to obtain thin sheets of siloxane scintillator, photographed in its main steps. From left to right: pouring of the resin with additives into the film applicator (500 μm gap), casting with motorized stage, immersion in water of the vulcanized material and stripping from the glass plate, ultimately leading to dried, self-supporting foil of siloxane scintillator ready to be cut to size.

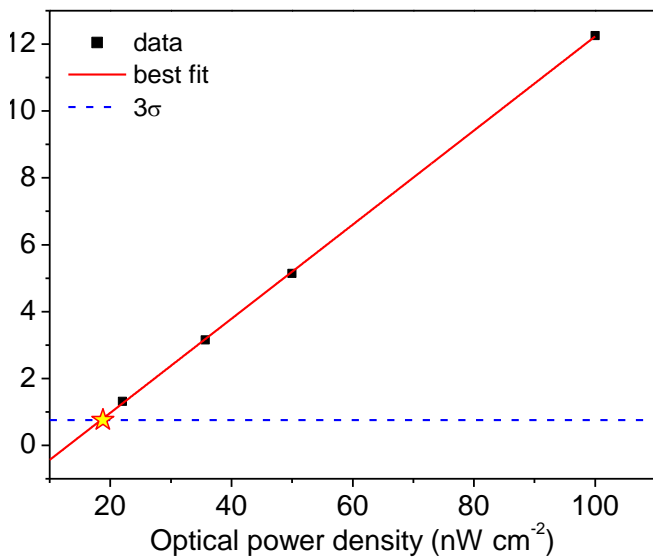


Supplementary Figure 5. Coupled siloxane scintillator with OPT. The polysiloxane based scintillating layer applied on the top of the OPT device with a thin layer of optical cement EJ-500 (Eljen Technology) assures a fast and robust bonding. Upon bending to the required curvature radius, it was not observed any detachment nor cracks.

Supplementary Note 3. Organic phototransistors

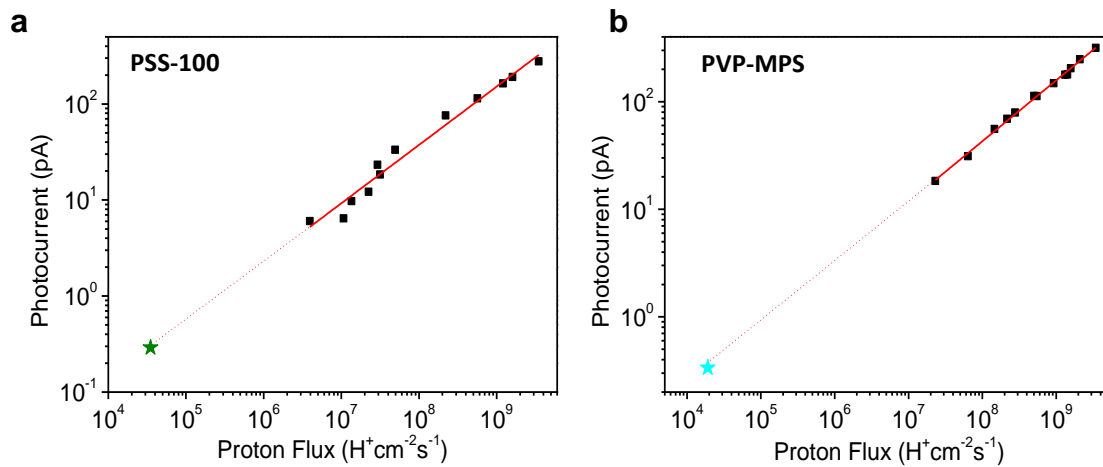


Supplementary Figure 6. OPT stability under bias stress. (a) The variation of the threshold voltage V_{TH} is reported for a device under either positive or negative bias stress. The stress time and bias are much longer and higher than the expected measurement time and operating conditions of the photodetector. (b) Transfer characteristics collected before and after the scintillator deposition on the OPT.



Supplementary Figure 7. Limit Of Detection estimation for the OPT under light at 460 nm wavelength. The measurements were performed with a light pulse width of 10s to emulate the operating conditions used during the measurements under proton beam irradiation.

Supplementary Note 4. Proton detector

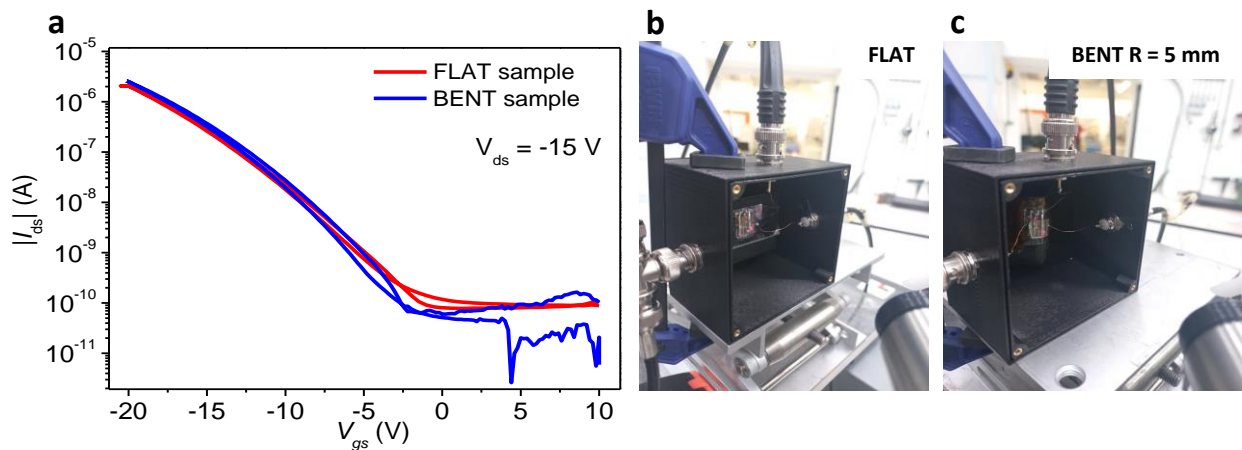


Supplementary Figure 8. Limit Of Detection estimation for the detector under proton irradiation. The values were calculated for the indirect detector with the scintillators based on PSS100 (a) and on PVP-MPS (b).

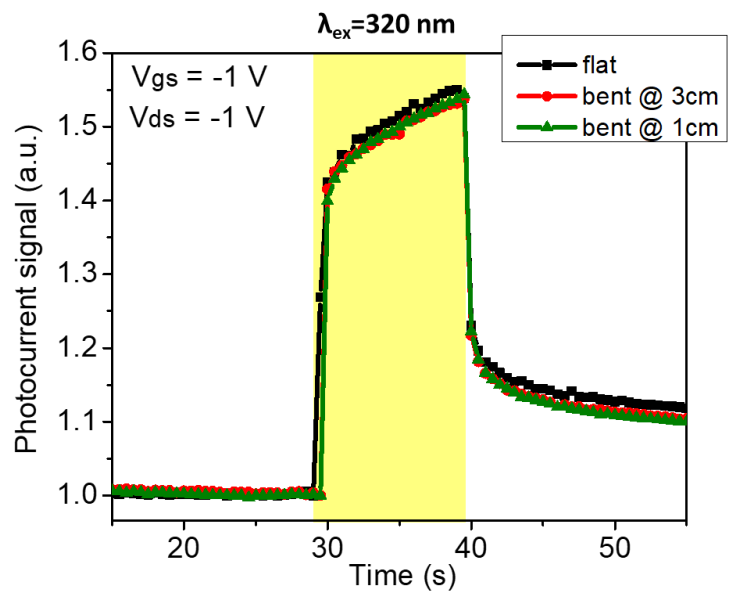
Proton sensor type	Dose rate detection limit (Gy min ⁻¹)	Dose rate operative range (Gy min ⁻¹)	Total dose applied range (Gy)	Notes	Ref.
Indirect, polysiloxane scintillator	0.026	1.2 ÷ 3.8×10 ³	0.2 ÷ 6×10 ²	Flexible, OPT photodetector, on-line reading	This work
Direct, organic semiconductors	18	240 ÷ 66×10 ³	40 ÷ 11×10 ²	Flexible, on-line reading	10
Indirect, polysiloxane composite with inorganic phosphors	N.A. ¹	56 ÷ 145	10, 17, 18 (fixed doses)	Radiochromic; off-line reconstruction	11
Indirect, alkali halides	N.A.	0.083 ÷ 0.5	0 ÷ 10	Scintillator; on-line reading	12
Indirect, optical fiber	0.0024	0.060 ÷ 3×10 ³	1 ÷ 1×10 ⁴	Silica optical fiber scintillator	13
Direct, Electrode type	N.A.	10 ÷ 40	2 ÷ -20	Patented, electrode type, in-vivo reading	14

¹Not Available

Supplementary Table 3. Comparison of operative range with recently reported SoA proton detectors.



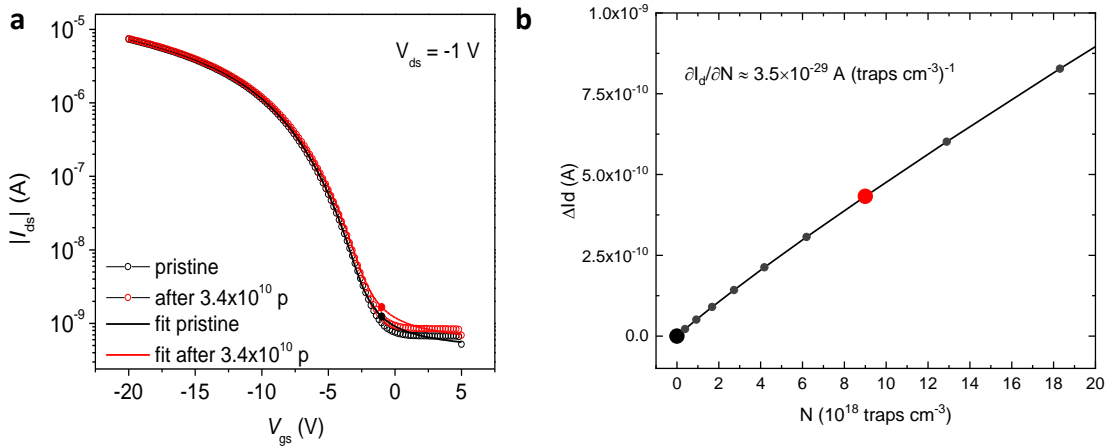
Supplementary Figure 9. Bending Test under proton beam. (a) OPT transfer characteristics of the flat (red curve) and bent (blue curve) samples employed for the bending test under proton beam. (b, c) 3D printed measurement chamber for the detector characterization in flat (b) and bent (c) configuration.



Supplementary Figure 10. Stability of the detector's response at different bending radii. Measurement the response of the same detector, kept flat and bent at different radii, upon exciting the scintillator by means of photons at $\lambda=320$ nm provided by a Xe lamp (150 W) coupled with a monochromator.

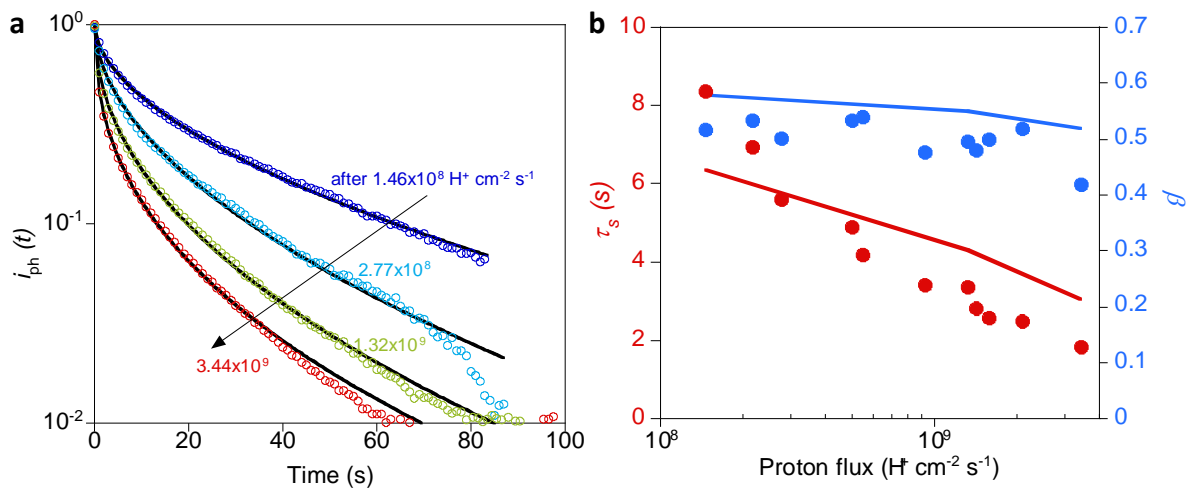
Supplementary Note 5. Kinetic model

Experimental



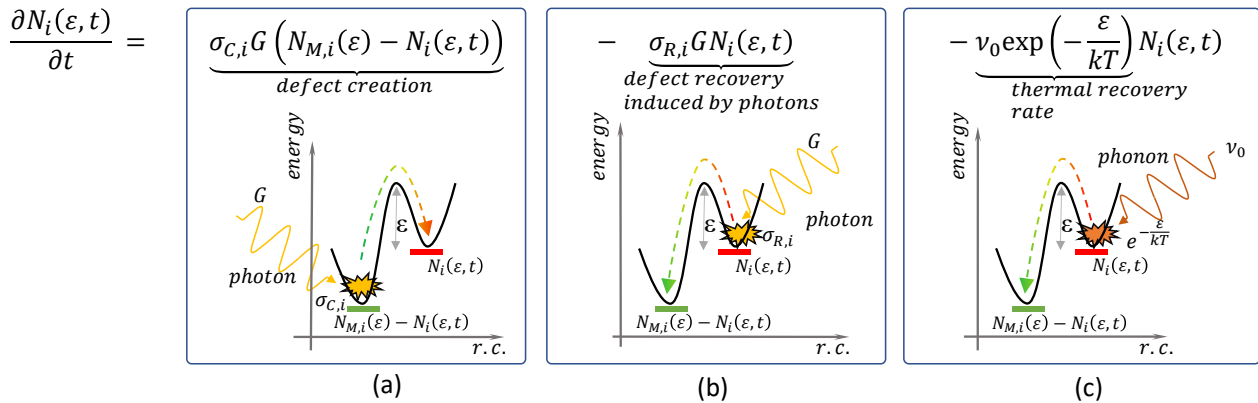
Supplementary Figure 11. Field-effect 1D simulation of the transfer characteristics before and after the proton

exposure. (a) Symbols: transfer characteristics of the OPT in proton detector measured before and after a dose of 3.4×10^{10} protons cm^{-2} (experimental data from Fig. 4d, reported here for reference); lines: fit of the transfer characteristics with the 1D model introducing deep trap states in the semiconductor energy gap. (b) Drain current variations as a function of the amount N of deep traps introduced following the exposure: the black and red dots correspond to the big red and black dots of panel (a).

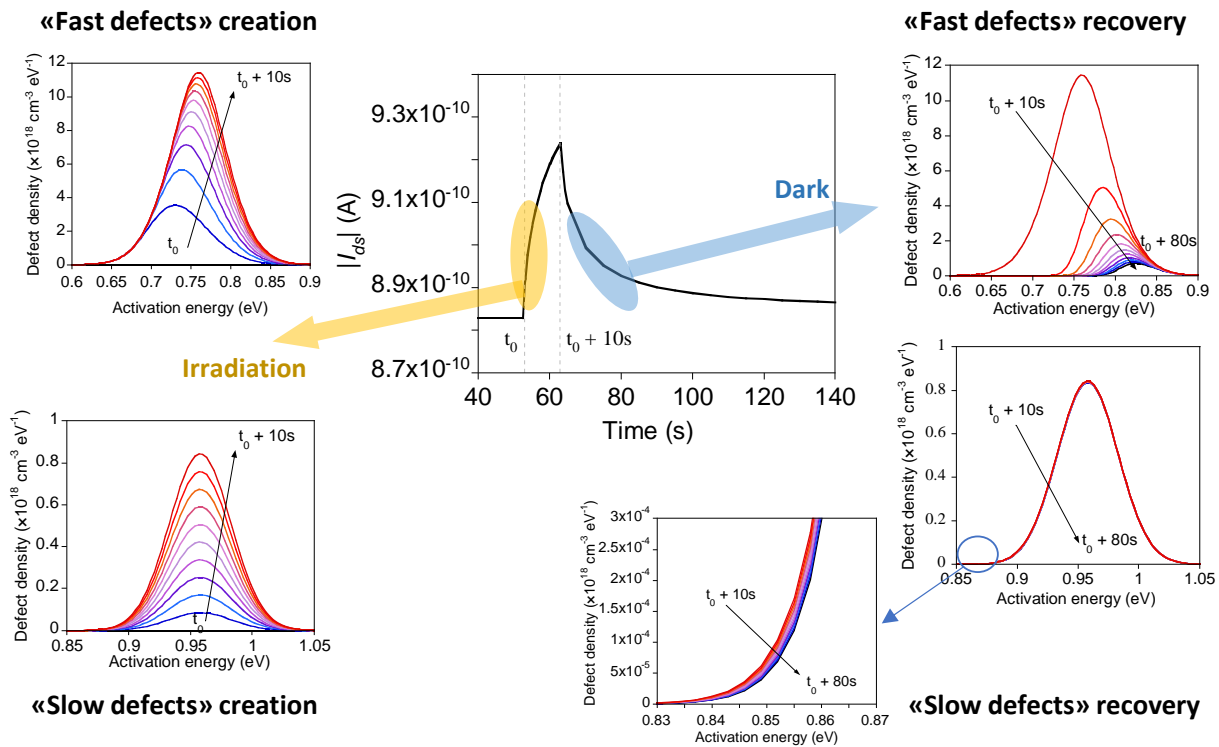


Supplementary Figure 12. Analyses of the relaxation in dark. (a) Symbols: normalized dynamic photocurrent relaxation $i_{\text{ph}}(t) = \frac{I_{\text{ph}}(t) - I_{\text{ph}}(\infty)}{I_{\text{ph}}(0) - I_{\text{ph}}(\infty)}$ measured after 10 s exposure to different proton flux on the indirect PVP-MPS detector. Continuous lines: fit with a stretched exponential relaxation function $i_{\text{ph}}(t) = \exp\left(-\left(\frac{t}{\tau_s}\right)^\beta\right)$. (b) Stretched exponential relaxation parameters as a function of the precedent proton flux exposure on indirect PVP-MPS detector extracted from experimental (symbols) and simulated data (lines).

General solution



Supplementary Figure 13. Schematic of the defect creation and recovery process. (a) Photon induced defect creation. (b) Photon induced defect recovery. (c) Phonon induced defect recovery. In the three panels, the black curves are a qualitative sketch of the potential energy profile as a function of a “reaction coordinate” (indicated by “r.c.” on the abscissae axis) that leads from the ground (undefected) state, indicated in green, to the defected state, in red. The three processes (a), (b), and (c) correspond to the three terms of the rate equation, reported above the plots. The quantities entering in the rate equations (described in the text) are also indicated in the sketch to better illustrate the underlying physics.



Supplementary Figure 14. Time evolution of the defect energy distribution during irradiation and in dark conditions. For better clarity, the distributions of fast- and slow-recovery defects are reported on different plots.

Following Street et. al¹⁵, we assumed that the driving force for defect creation is the photon flux impinging on the organic semiconductor, while defect recovery can be photon- or thermally-induced. In Supplementary Figure 13 panel (a), there is a qualitative schematic of the defect creation process as is assumed in the kinetic model: a photon interacts on a site of an organic semiconductor molecule, triggering the creation of a defect that is electrically active. We can qualitatively describe the energetics of this process with a “reaction coordinate” (indicated by “r.c.” in the plots) going from the undefected ground state, represented by the green line, to the defected state with a higher potential energy, indicated by the red line. We assume that the potential energy as a function of the reaction coordinate has a maximum between the ground and defected states coordinate, and that the energy difference between the maximum and the ground state is lower than the energy of the impinging photons. In this way, we can describe the creation rate of defected states by introducing a photon/ground state cross section. Similarly, in Supplementary Figure 13 panel (b), the photon induced defect recovery process, involving a photon/defected state cross section, is depicted. In Supplementary Figure 13 panel (c) the thermally induced defect recovery process is schematized: this time, the interaction between phonons and defected states is weighted by the Boltzmann factor accounting for the probability of a thermal fluctuation with energy higher than the difference between the maximum and the defect state energy. For the sake of clarity, the plots of Supplementary Figure 13 refer to the creation or recovery of a single defected state: as discussed in the main text, the experimental evidence strongly suggest that the defected states have recovery energies distributed with a density given by the sum of two Gaussian with different mean values and variances (see main text), identifying fast- and slow-recovery defects.

By summing the three contributions to the net defect creation rate, we obtain the following equation:

$$\frac{\partial N_i(\varepsilon, t)}{\partial t} = \underbrace{\sigma_{C,i} G (N_{M,i}(\varepsilon) - N_i(\varepsilon, t))}_{\text{defect creation}} - \underbrace{\frac{\sigma_{R,i} G N_i(\varepsilon, t)}{\text{defect recovery induced by photons}}}_{\text{defect recovery induced by photons}} - \underbrace{v_0 \exp\left(-\frac{\varepsilon}{kT}\right) N_i(\varepsilon, t)}_{\text{thermal recovery rate}} \quad (1)$$

The index i identify the kind of defects ($i = 1$ fast recovery defects, related to the swift photoresponse component - $i = 2$ slow recovery defects, related to the persistent photoresponse component), ε is the recovery activation energy ($\varepsilon > 0$), $N_i(\varepsilon, t)$ is the instantaneous defect energy distribution at time t , G is the photon flux (units: [photons $\text{cm}^{-2} \text{s}^{-1}$]), $\sigma_{C,i}$ is the photon cross section for defect creation (undefected + photon => defected), $\sigma_{R,i}$ is the photon cross section for defect recovery (defected + photon => undefected), and ν_0 is the typical phonon frequency (around 1 THz). The density of sites $N_{M,i}(\varepsilon)$ that can host a defect of type i with an activation energy ε is assumed to have a gaussian distribution with mean value ε_i , variance δ_i , and total integral $N_{T,i}$ (see Fig. 5D).

$$N_{M,i}(\varepsilon) = \frac{N_{T,i}}{\sqrt{2\pi}\delta_i} \exp\left[-\frac{1}{2}\left(\frac{\varepsilon - \varepsilon_i}{\delta_i}\right)^2\right] \quad (2)$$

Numerical solution of Eq. 1 leads to the determination of $N_i(\varepsilon, t)$ as shown in Supplementary Figure 13. Hence $N(t)$ is computed as:

$$N(t) = \sum_i \int N_i(\varepsilon, t) d\varepsilon \quad (3)$$

Once $N(t)$ is known, by using Eq. 3 of main text $I_{\text{ph}}(t)$ can be computed.

The numerical values of the parameters appearing in the model were determined by fitting the dynamical photoresponses of the OPT under light exposure and the detector (with PVP-MPS scintillator) under proton irradiation. The model parameters have been estimated by using the Levenberg–Marquardt method for the minimization of the least-squares error between the experimental dynamical curves and the computed ones.

All the dynamical curves were fitted by using the same parameters values for properties related to intrinsic characteristics of the organic semiconductor ($N_{T,i}$, ε_i , and δ_i), whose values determines the distributions shown in Fig. 5d. We note that the overall (integrated) amount of type $i = 1$ defects, peaked around $\varepsilon_1 = 0.707$ eV, is twice the overall amount of type $i = 2$ defects, peaked

around $\varepsilon_2 = 0.958$ eV, indicating a decreasing trend of the amount of defect as a function of their recovery energy. On the other hand, the values of the parameters related to the interaction of the OSC with the radiation (the cross sections $\sigma_{C,i}$ and $\sigma_{R,i}$, see Supplementary Table 3) were adjusted according to the specific configuration being fitted. In fact, while monochromatic light with a wavelength tuned in correspondence of the absorption peak of DNTT was used for the optical response measurements shown in Fig. 5a, the IBIL spectra of scintillators has a larger wavelength distribution (Fig. 2a) and different effective couplings between OSC and light were expected in the two cases.

Eq. 1 has the form:

$$\frac{dy}{dt} = a - by(t) \quad (4)$$

with:

$$a \equiv \sigma_{C,i}GN_{M,i}(\varepsilon) \quad (5)$$

$$b \equiv (\sigma_{C,i} + \sigma_{R,i})G + \nu_0 \exp\left(-\frac{\varepsilon}{kT}\right) \quad (6)$$

$$y(t) \equiv N_i(\varepsilon, t) \quad (7)$$

After a time Δt after t_0 the solution evolves according to:

$$y(t_0 + \Delta t) = \frac{a}{b} - \left(\frac{a}{b} - y(t_0)\right) \exp(-b\Delta t) \quad (8)$$

An example of the time evolution of the two defects energy distributions under illumination and recovery in dark is reported in Supplementary Figure 14.

The quantity b is identified as the reciprocal of the characteristic time $\bar{T}_i = 1/b$ governing the creation or the relaxation dynamics of the defects, and it depends on the instantaneous light flux G and on the recovery activation energy ε of the defect, $\bar{T}_i = \bar{T}_i(G, \varepsilon)$.

For times long enough, $N_i(\varepsilon, t)$ reaches the steady state value:

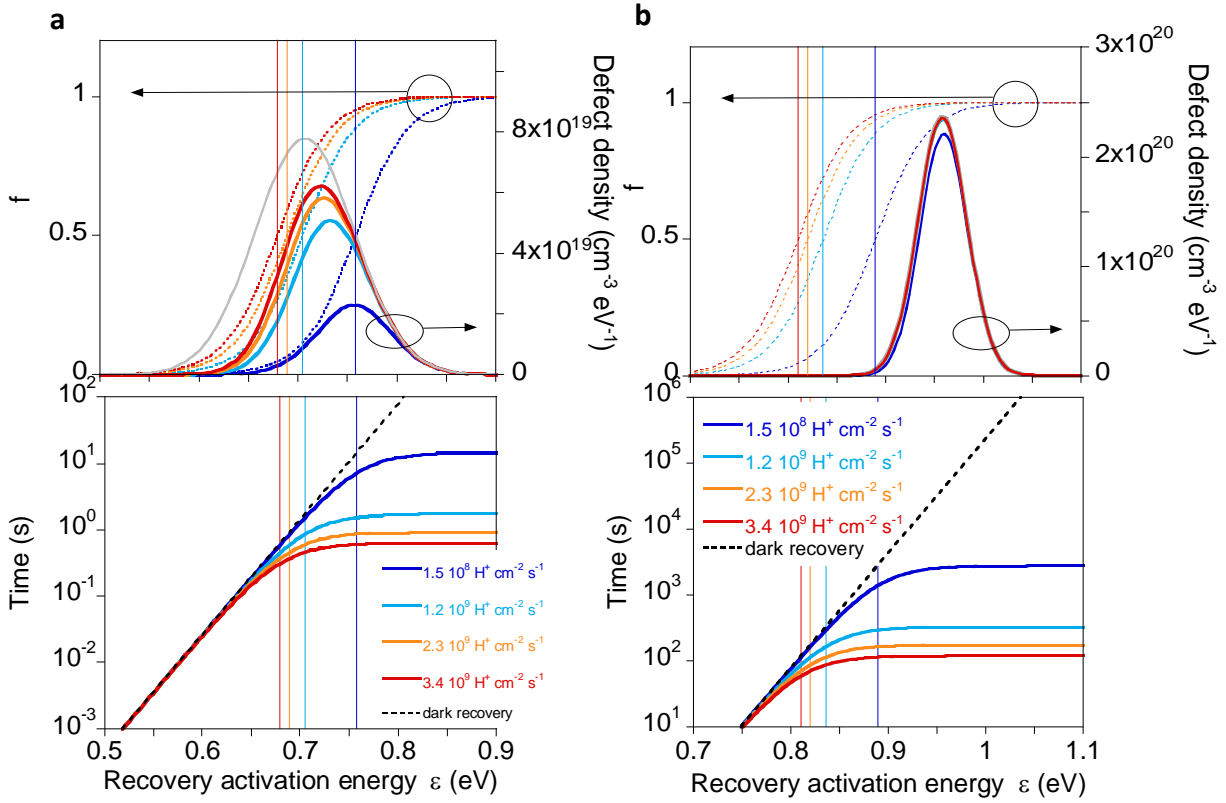
$$N_i(\varepsilon, \infty) = \frac{\sigma_{C,i}G}{(\sigma_{C,i} + \sigma_{R,i})G + \nu_0 \exp\left(-\frac{\varepsilon}{kT}\right)} N_{M,i}(\varepsilon) \quad (9)$$

with a characteristic time

$$\bar{T}_i(G, \varepsilon) = \frac{1}{(\sigma_{C,i} + \sigma_{R,i})G + \nu_0 \exp\left(-\frac{\varepsilon}{kT}\right)} \quad (10)$$

Equations (9) and (10) explain the increasing non-linearity of the photoresponse at high irradiance and long exposure times, shown in the inset of Fig. 3d. In fact, Eq. (9) predict an almost linear relationship between $N_i(\varepsilon, \infty)$ and G at low irradiances (that is, when $(\sigma_{C,i} + \sigma_{R,i})G$ is negligible w.r.t $\nu_0 \exp\left(-\frac{\varepsilon}{kT}\right)$), and becomes increasingly sub-linear for increasing G . Moreover, the time needed to reach this steady state regime, \bar{T}_i , decrease with G (see Eq. (10)) thus explaining the non-linearity seen for longer exposure times at higher irradiances.

Analysis



Supplementary Figure 15. Steady state defect energy distributions and characteristic times.

Steady state defect energy distributions (upper plots) and creation/recovery characteristic times (lower plots) computed for fast-recovery (a) and slow-recovery (b) defects in proton detectors (PVP-MPS). Computations have been made for different proton fluxes (see color legend). Also shown the defect energy distributions for very high proton flux (gray line) and the Fermi-like functions f governing the dependence upon the flux (dashed thin lines). The vertical thin lines indicate the energies $\bar{\varepsilon}_i(G)$ (see text).

For a photon flux $G > 0$, it is useful to define the energy $\bar{\varepsilon}_i(G)$ such that:

$$\bar{\varepsilon}_i(G) = kT \log \left(\frac{\nu_0}{(\sigma_{C,i} + \sigma_{R,i})G} \right) \quad (11)$$

so that Eq. 9 can be cast in the form:

$$N_i(\varepsilon, \infty) = \frac{\sigma_{C,i}}{\sigma_{C,i} + \sigma_{R,i}} f(\varepsilon - \bar{\varepsilon}_i(G)) N_{M,i}(\varepsilon) \quad (12)$$

where the function

$$f(\varepsilon - \bar{\varepsilon}_i(G)) = \frac{1}{1 + \exp\left(-\frac{\varepsilon - \bar{\varepsilon}_i(G)}{kT}\right)} \quad (13)$$

has been introduced. The function $f(\varepsilon - \bar{\varepsilon}_i(G))$ has the same functional form of the Fermi function (for holes) with $\bar{\varepsilon}_i(G)$ playing the role of a fictitious “light flux dependent chemical potential”.

Hence, the defect energy distribution, $N_i(\varepsilon, t)$, in the limit of long exposure times is:

$$\text{for } \varepsilon \ll \bar{\varepsilon}_i(G) \Rightarrow N_i(\varepsilon, \infty) \rightarrow 0$$

$$\text{for } \varepsilon \gg \bar{\varepsilon}_i(G) \Rightarrow N_i(\varepsilon, \infty) \rightarrow \frac{\sigma_{C,i}}{(\sigma_{C,i} + \sigma_{R,i})} N_{M,i}(\varepsilon)$$

In the upper panels of Supplementary Figure 15a and Supplementary Figure 15b, $f(\varepsilon - \bar{\varepsilon}_i(G))$ and the resulting $N_i(\varepsilon, \infty)$ are plotted together for different values of G as a function of ε : it is apparent that, as the light flux is increased, $\bar{\varepsilon}_i(G)$ shifts towards lower values. If $\bar{\varepsilon}_i(G)$ is located near ε_i , as it happens in the case $i = 1$ (fast-recovery defects), then an increase in light flux determines also a growth of the steady defect distribution, with a shift of its peak toward lower energies (see Supplementary Figure 15a). Recalling that the energy of the peak of the distribution can be related to the characteristic time τ_s of the stretched exponential relaxation¹⁶, we can attribute to this shift the reduction of τ_s for increasing light flux exposures (see Supplementary Figure 12b).

The characteristic times for the creation of defects under illumination are plotted for different values of G as a function of ε in the lower plots of Supplementary Figure 15a and 15b for fast- and slow-recovery defects, respectively.

- For energies ε lower than $\bar{\varepsilon}_i(G)$ we have lower values for $\bar{T}_i(G, \varepsilon)$, but, in this case, the steady state defect density, $N_i(\varepsilon, \infty)$, is negligible due to the vanishing of $f(\varepsilon - \bar{\varepsilon}_i(G))$.

This means that the defects created by photons in this energy range are rapidly annealed by thermal agitation.

- For energies ε higher than $\bar{\varepsilon}_i(G)$, $\bar{T}_i(G, \varepsilon)$ is determined by the light flux and reduces for increasing G . If in this energy range $N_i(\varepsilon, \infty)$ is appreciably higher than zero, then the light flux actually creates defects with a dynamic that is speeded up by increasing G .

Due to the smaller values of the cross sections $\sigma_{C,i}$ and $\sigma_{R,i}$ associated with the slow-recovery defects, we note that the characteristic times for these defects are considerably longer than those associated to fast-recovery defects: in the range of flux probed in this work, the time needed to reach steady state conditions for $\varepsilon \gg \bar{\varepsilon}_i(G)$ ranges from 2800 s to 120 s for slow-recovery defects while it is in the range of 15-0.6 s for fast-recovery defects. This means that in the exposure conditions used in this work the slow-recovery defects never reach steady state conditions but increases after each exposure determining the “staircase” behavior due to the buildup of a persistent photocurrent.

Returning to Eq. 9, we have in dark conditions $G = 0$ and $N_i(\varepsilon, t)$ relax to 0 with a characteristic time

$$\bar{T}_i(G = 0, \varepsilon) = \frac{1}{\nu_0} \exp\left(+\frac{\varepsilon}{kT}\right) \quad (14)$$

that increase exponentially with the activation energy. In the lower plots of Supplementary Figure 15a and 15b it is reported $\bar{T}_i(G = 0, \varepsilon)$ (dark recovery) as a function of ε : it is apparent that for $\varepsilon \gg \bar{\varepsilon}_i(G)$ the time needed to recover a defect is sensibly higher than the time needed to create it resulting in a persistent photocurrent.

Cross sections	Detector (PVP-MPS) [cm ² per photons]	OPT [cm ² per photons]
$\sigma_{C,i=1}$	$(3.98\pm0.06)\times10^{-16}$	$(1.432\pm0.003)\times10^{-15}$
$\sigma_{R,i=1}$	$(9.3\pm0.4)\times10^{-15}$	$(6.57\pm0.03)\times10^{-14}$
$\sigma_{C,i=2}$	$(1.0\pm0.2)\times10^{-17}$	$(4.56\pm0.02)\times10^{-17}$
$\sigma_{R,i=2}$	$(3.8\pm0.2)\times10^{-16}$	$(2.28\pm0.02)\times10^{-15}$

Supplementary Table 4. Cross sections values estimated by best fit of the experimental curves for the OPT under light exposure and the detector under proton irradiation.

Supplementary References

1. Dalla Palma, M., Quaranta, A., Marchi, T., Collazuol, G., Carturan, S., Cinausero, M., Degerlier, M. & Gramegna, F. Red Emitting Phenyl-Polysiloxane Based Scintillators for Neutron Detection. *IEEE Trans. Nucl. Sci.* **61**, 2052–2058 (2014).
2. Pandey, A. K., Shaw, P. E., Samuel, I. D. W. & Nunzi, J.-M. Effect of metal cathode reflectance on the exciton-dissociation efficiency in heterojunction organic solar cells. *Appl. Phys. Lett.* **94**, 103303 (2009).
3. Yamada, K., Suzuki, M., Suenobu, T. & Nakayama, K. High Vertical Carrier Mobilities of Organic Semiconductors Due to a Deposited Laid-Down Herringbone Structure Induced by a Reduced Graphene Oxide Template. *ACS Appl. Mater. Interfaces* **12**, 9489–9497 (2020).
4. An, Q., Zhang, F., Li, L., Wang, J., Zhang, J., Zhou, L. & Tang, W. Improved Efficiency of Bulk Heterojunction Polymer Solar Cells by Doping Low-Bandgap Small Molecules. *ACS Appl. Mater. Interfaces* **6**, 6537–6544 (2014).
5. Long, Y., Ward, A. J., Ruseckas, A. & Samuel, I. D. W. Effect of a high boiling point additive on the morphology of solution-processed P3HT-fullerene blends. *Synthetic Metals* **216**, 23–30 (2016).
6. Calvi, S., Rapisarda, M., Valletta, A., Scagliotti, M., De Rosa, S., Tortora, L., Branchini, P. & Mariucci, L. Highly sensitive organic phototransistor for flexible optical detector arrays. *Organic Electronics* **102**, 106452 (2022).

7. Milvich, J., Zaki, T., Aghamohammadi, M., Rödel, R., Kraft, U., Klauk, H. & Burghartz, J. N. Flexible low-voltage organic phototransistors based on air-stable dinaphtho[2,3-b:2',3'-f]thieno[3,2-b]thiophene (DNFTT). *Organic Electronics* **20**, 63–68 (2015).
8. Pierre, A., Gaikwad, A. & Arias, A. C. Charge-integrating organic heterojunction phototransistors for wide-dynamic-range image sensors. *Nature Photon* **11**, 193–199 (2017).
9. Funt, B. L. & Hetherington, A. Spiral Capillary Plastic Scintillation Flow Counter for Beta Assay. *Science* **129**, 1429–1430 (1959).
10. Fratelli, I., Ciavatti, A., Zanazzi, E., Basiricò, L., Chiari, M., Fabbri, L., Anthony, J. E., Quaranta, A. & Fraboni, B. Direct detection of 5-MeV protons by flexible organic thin-film devices. *Science Advances* **7**, (2021).
11. Valdetaro, L. B., Høye, E. M., Skyt, P. S., Petersen, J. B. B., Balling, P. & Muren, L. P. Empirical quenching correction in radiochromic silicone-based three-dimensional dosimetry of spot-scanning proton therapy. *Physics and Imaging in Radiation Oncology* **18**, 11–18 (2021).
12. Setianegara, J., Mazur, T. R., Yang, D. & Li, H. H. Dual-storage phosphor proton therapy dosimetry: Simultaneous quantification of dose and linear energy transfer. *Medical Physics* **48**, 1941–1955 (2021).
13. Girard, S., Di Francesca, D., Morana, A., Hoehr, C., Paillet, P., Duzenli, C., Kerboub, N., Reghioua, I., Li Vecchi, G., Alessi, A., Duhamel, O., Trinczek, M., Marin, E., Boukenter, A., Ouerdane, Y., Mekki, J., Garcia Alia, R., Kadi, Y. & Brugger, M. X-Rays, γ -Rays, and Proton Beam Monitoring With Multimode Nitrogen-Doped Optical Fiber. *IEEE Transactions on Nuclear Science* **66**, 306–311 (2019).
14. Cirrone, G. A. P., Amato, N., Catalano, R., Di Domenico, A., Cuttone, G., Lojacono, P., Mazzaglia, A., Pace, F., Pittà, G., Raffaele, L., Salamone, V., Spatola, C. & Petringa, G. On the Possibility to Use the Charge Imbalance in Patients Undergoing Radiotherapy: A New Online, In Vivo, Noninvasive Dose Monitoring System. *Applied Sciences* **11**, 7005 (2021).

15. Street, R. A., Yang, Y., Thompson, B. C. & McCulloch, I. Capacitance Spectroscopy of Light Induced Trap States in Organic Solar Cells. *J. Phys. Chem. C* **120**, 22169–22178 (2016).
16. Edholm, O. & Blomberg, C. Stretched exponentials and barrier distributions. *Chemical Physics* **252**, 221–225 (2000).